

In-situ Optimization of Acoustic Hologram with Digital Twin

Tatsuki Fushimi^{1,2*}, Daichi Tagami³, Kenta Yamamoto³
and Yoichi Ochiai^{1,2,4}

^{1*}Institute of Library, Information and Media Science, University
of Tsukuba, Kasuga Campus Kasuga 1-2, Tsukuba, 305-8550,
Ibaraki, Japan.

²R&D Center for Digital Nature, University of Tsukuba, Kasuga
Campus Kasuga 1-2, Tsukuba, 305-8550, Ibaraki, Japan.

³Graduate School of Comprehensive Human Sciences, University
of Tsukuba, Kasuga Campus Kasuga 1-2, Tsukuba, 305-8550,
Ibaraki, Japan.

⁴Pixie Dust Technologies, Inc., Misakicho 2-20-5, Chiyoda,
101-0061, Tokyo, Japan.

*Corresponding author(s). E-mail(s): tfushimi@slis.tsukuba.ac.jp;

Keywords: Acoustic Hologram, Acoustic Levitation, Acoustophoretic
Volumetric Display, Optimization

Abstract

As the use of acoustophoresis methods such as ultrasonic haptic sensation, acoustic levitation, acoustic streamings, and displays becomes more prevalent, the need for the accurate generation of acoustic holograms has increased. However, experimental results have shown that the actual acoustic field may differ from the simulated field owing to uncertainties in the transducer position, power and phase, or from nonlinearity and inhomogeneity in the field. Traditional methods for experimentally optimizing acoustic holograms require prior calibration and do not scale well with the number of variables. Our proposed digital twin approach combines feedback from experimental measurements in the physical setup with numerically obtained derivatives of the loss function using automatic differentiation to optimize the loss function. This approach is faster and more efficient than the classical finite difference approach, making it beneficial for various applications such as acoustophoretic volumetric displays, ultrasonic haptic sensations, focused ultrasound therapy, and non-destructive testing.

Recent advances in acoustophoresis, such as the development of ultrasonic haptic sensation[1, 2], acoustic levitation[3–5], acoustic streamings[6, 7], and displays [8–11], have caused an increased need for the accurate generation of acoustic holograms. A number of acoustic hologram optimization techniques have been proposed, including Gerchberg-Saxton[12–14], Eigensolver and Tikhonov-regularization[2], machine learning methods[15, 16], direct solvers[17], and greedy-type solvers[18]. In 2021, we demonstrated an automatic differentiation approach to acoustic hologram optimization[19, 20] and exhibited good accuracy with the use of automatic differentiation and the Adam optimizer.

While these numerical approaches use simulated values to optimize acoustic fields, a number of experimental results suggest that the acoustic field in reality is offset from the numerically simulated field [3, 8, 21–23]. These offsets could emerge from simple uncertainties in the transducer position, power, and phase, or they could emerge from non-linearity, inhomogeneity, or the existence of other scatterers in the field. Recent advances in computational modeling have started to enable the inclusion of complex nonlinear fields produced by acoustic holograms [24], or complex fields with scatterers in the field [9, 25]. However, it is still computationally expensive and cumbersome to include nonlinearity, and experimental deviations are susceptible to minor changes in the environment.

Some attempts have already been made to experimentally optimize acoustic holograms [8, 23, 26]. For example, the offset of equilibrium points could be addressed by calibrating the focal points with the equilibrium position of the levitated particles [26], or by the combination of a gradient descent algorithm and experimentally obtained finite differences [8]. While these optimizers are effective in achieving their targets, they require prior calibration, or experimental finite differences that do not scale well with the number of variables. These experimental deviations are known to cause performance degradation in the practical applications of acoustic holograms [8, 22, 24], and there is an increasing need for better and more efficient approaches to optimize acoustic holograms in experiments.

Herein, we propose a digital twin approach for optimizing the acoustic holograms, as shown in Fig. 1. Experimental measurements in situ (physical setup) are fed back into the loss function of the optimizer, and the digital model of the experimental setup is used to obtain the gradient of the loss function with respect to each variable using automatic differentiation. Because the gradient of the loss function is approximated numerically from the digital model, there is no need for the experimental finite difference algorithm. Thus, the optimizer will complete its optimization at least the “number of variables” times faster than the classical finite difference approach. Digital twin optimization is highly beneficial in PAT application because the number of transducers are in the magnitude of 10^2 to 10^3 (i.e. up to 10^3 times faster). Considering the fact that the optimization is performed iteratively, this brings significant enhancement of the performance and efficiency. Such methods that are used to connect experimental to digital models have been proven to be effective in machine

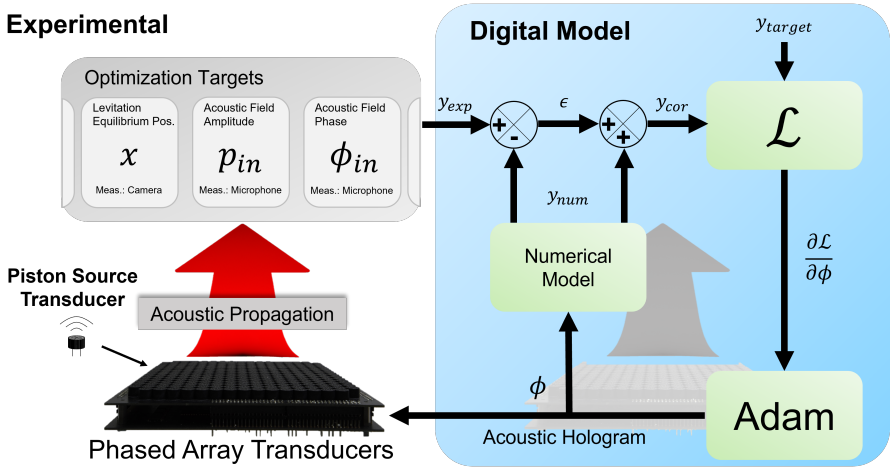


Fig. 1 In-situ optimization with digital twin. Acoustic hologram is passed on to both the experimental setup, and numerical model. Both propagates the hologram in experiment and numerical simulation. The optimization targets can be anything that can be physically measured and modelled. The experimental measurements can be made via various instruments such as cameras, microphones, or laser doppler vibrometers. After taking the experimental measurements, the difference (ϵ) between the experimental data (y_{exp}) and numerical data (y_{num}) is fed in, and added together to form a corrected value (y_{cor}). The corrected value is fed into the automatic differentiation package, and the solutions are updated accordingly using stochastic gradient descent algorithms.

learning [27], and optics [28]; the application of this method in acoustic hologram could be beneficial in acoustophoretic volumetric displays, ultrasonic haptic sensations, focused ultrasound therapy, and non-destructive testings.

The core of the optimization algorithm is the Diff-PAT; an acoustic hologram optimization method based on automatic differentiation is demonstrated by Fushimi et al. [19]. The initial guess of the acoustic hologram is updated iteratively using the Adam optimizer based on the differentiated value of loss with respect to each phase of the transducers. The Adam optimizer iteratively updates the initial guess of the variables (θ_t) by:

$$\theta_t = \theta_{t-1} - \alpha \cdot \frac{\hat{m}_t}{\sqrt{\hat{v}_t + \epsilon}} \quad (1)$$

where θ is the optimization variable, and subscript t is the step number. $\hat{v}_t = \frac{v_t}{1-\beta_2^t}$, $\hat{m}_t = \frac{m_t}{1-\beta_1^t}$, $v_t = \beta_2 \cdot v_{t-1} + (1-\beta_2) \cdot g_t^2$, $m_t = \beta_1 \cdot m_{t-1} + (1-\beta_1) \cdot g_t$, and $g_t = \frac{\delta L_t(\theta_{t-1})}{\delta \theta}$. Here, α is the step size/learning rate, $\beta_1 = 0.9$, $\beta_2 = 0.999$, and $\epsilon = 1 \times 10^{-7}$ are exponential decay rates for the moment estimates. We adjusted the learning rates depending on each application, and the used value was specified within each case.

As shown above, the Adam optimizer only uses the derivative of the loss function ($L_t(\theta_{t-1})$) to update the parameters. Naturally, the question arises on “how can it know which way to descend to in the experiment when it only

uses a gradient that is numerically obtained?” In a nutshell, we design the loss function such that “the experimentally obtained states carry over to the derivative of the loss function”, and when it does, “the gradient at the target state is steep”. Thus, when the loss function is properly designed; the Adam optimizer determines the minima at the target state in the experiments.

For example, a loss function could be specified as $L_t(\theta_{t-1}) = (T - f_{exp}(\theta_{t-1}))^2$, where T is the target value (i.e. target acoustic pressure, phase, or equilibrium position), and subscript “exp” means experimentally obtained. When differentiated, the function becomes $\frac{\delta L_t}{\delta \theta_t} = -2(L - f_{exp}(\theta_{t-1}))\frac{\delta f_{num}(\theta_{t-1})}{\delta \theta}$ with subscript “num” denoting a numerically obtained value. Thus, the experimentally optimum point naturally becomes the destination of the Adam optimizer. The optimization target can be anything that can be physically measured and predicted in in-situ optimization. In this study, we demonstrate the optimization of the (i) acoustic pressure, and (ii) equilibrium position to demonstrate the relevance of digital twin optimization in PAT and acoustic holograms in general. Finally, we discuss the design of the loss function in the discussion section.

First, we describe digital twin optimization for the acoustic pressure field. We use PAT as described in the Methods section, and it takes phase only acoustic holograms (operates in phase-only A mode hologram). As in Fushimi et al. [20], we begin by defining a suitable loss function for the phase-only (A:i), amplitude only (A:ii), and phase and amplitude (A:iii) optimization:

$$L(\phi_t) = [(A_c \cos \phi_c - A_p^{exp} \cos(\phi_p^{exp}))^2 + (A_c \sin \phi_c - A_p^{exp} \sin(\phi_p^{exp}))^2], \quad (2)$$

where A_c and ϕ_c are the target pressure amplitude and phase, and $A_p^{exp}(x, x_t, \phi_t) = |p_{in}(x, x_t, \phi_t)| + G(p_{exp} - |p_{in}(x, x_t, \phi_t)|)$ and $\phi_p^{exp} = \arg(p_{in}(x, x_t, \phi_t)) + G(\phi_{exp} - \arg(p_{in}(x, x_t, \phi_t)))$ are substituted pressure amplitude and phase, respectively. The substituted pressure amplitude allows the automatic differentiation package (in this case TensorFlow) to track the gradient of the function, whereas the inside of function $G()$ is untracked by the package (achieved by for e.g. `tf.stop_gradient()` in TensorFlow). As in Fushimi et al. [20], $A_c = 1$ was set for A:i and $\phi_c = 0$ was set for A:ii.

The experimentally obtained values (such as p_{exp} and ϕ_{exp}) are obtained using a calibrated pressure microphone (B&K Type 4138-A-015, pressure sensitivity $p_{sens}^{mic} = 1.0 \text{ mV Pa}^{-1}$), as detailed in the Methods section. Twenty target phase and amplitudes were set ($S = 20$) with a constant focal point, $x = (0, 0, 0.04) \text{ m}$. The phase linearly increased from 0 to 2π , and the amplitude increased linearly from 10 to 90% of p_{max} . p_{max} was set as the pressure amplitude with a single focus point in numerical simulation. The maximum iteration number was set to 100. The experimental measurements and optimizations were repeated 3 times ($S = 3$) to obtain the mean and standard deviation of the pressure and amplitude. The statistical analysis was performed on Matlab R2022a. The mean phase was obtained by $\phi_{mean} = \arctan\left(\frac{\sum_s^S \sin(\phi_{meas}^s)}{\sum_s^S \cos(\phi_{meas}^s)}\right)$ where ϕ_{meas} is the measured phase.

We can also apply the in-situ digital optimization for the equilibrium position of the levitated particle. While the acoustic pressure field can be calculated easily using Huygens' approach, the determination of the equilibrium position requires the balancing of the acoustic radiation force and gravity. This calculation requires a root-finding algorithm that iteratively updates its guess. Here, we use the single-axis acoustic levitator (2 SonicSurface array separated by a distance of 0.215 m). The target equilibrium shape was set to be a circle with radius $r = 3$ mm: $\mathbf{x}_f^t = (0, r \sin(q), 0.0119 + r + r \cos(q))$, where $q = \{r : r = \pi + \frac{2\pi}{29}n, n \in \{0, 1, \dots, 28\}\}$. While it is possible to optimize the equilibrium position from the acoustic hologram as in pressure field optimization, the levitation conditions are not necessarily guaranteed for all possible phase combinations. Thus, the optimization variable was constrained to known stable solutions using a single focal point and twin trap [4]:

$$\phi_t = \phi_{focal} + \phi_{twin}, \quad (3)$$

where $\phi_{focal} = -\frac{2\pi f_0}{c_0} [d(\mathbf{x}_f, \mathbf{x}_t) - d(0, \mathbf{x}_f)]$, and ϕ_{twin} are 0 and π for the bottom and upper arrays, respectively. As in a previous study[8], the target shape was specified using the focal points, and the equilibrium positions were recorded (waited 2.5 s after sending the commands to PAT for the steady state) using optical methods as described in the Methods section.

For a spherical particle in the Rayleigh regime ($r \ll \lambda$), the acoustic radiation force was calculated using Gor'kov [29, 30]:

$$\begin{bmatrix} F_x \\ F_y \\ F_z \end{bmatrix} = -\frac{4\pi}{3} a^3 \nabla \left[\frac{1}{2} \text{Re}[f_1] \kappa_0 \langle p_{in}(x, \phi_t)^2 \rangle - \frac{3}{4} \text{Re}[f_2] \rho_0 \langle v_{in}(x, \phi_t)^2 \rangle \right] \quad (4)$$

where $f_1 = 1 - \tilde{\kappa}$ and $f_2 = \frac{2(\tilde{\rho}-1)}{2\tilde{\rho}}$. $\tilde{\kappa} = \frac{\kappa_p}{\kappa_0}$ and $\tilde{\rho} = \frac{\rho_p}{\rho_0}$. Subscript 0 and p represent surrounding media and particle property, and $\kappa = \frac{1}{\rho c^2}$ where ρ and a are the density and radius of sphere, respectively. $v_{in}(x, \phi_t) = \left| \nabla \left(\frac{p_{in}}{\rho_0 \omega i} \right) \right|$ is the acoustic velocity field. Moreover, the particle property was arbitrarily set $a = 0.7\text{mm}$, $\rho_p = 40 \text{ kg m}^{-3}$, and $c_p = 900 \text{ m s}^{-1}$.

To determine the equilibrium position, a root finding algorithm (Newton gradient descent) was used [26]:

$$\mathbf{x}_e^{n+1} = \mathbf{x}_e^n - J^{-1} [F_x, F_y, F_z^g] \quad (5)$$

where $J = \begin{bmatrix} \frac{\delta F_x}{\delta x} & \frac{\delta F_x}{\delta y} & \frac{\delta F_x}{\delta z} \\ \frac{\delta F_y}{\delta x} & \frac{\delta F_y}{\delta y} & \frac{\delta F_y}{\delta z} \\ \frac{\delta F_z^g}{\delta x} & \frac{\delta F_z^g}{\delta y} & \frac{\delta F_z^g}{\delta z} \end{bmatrix}$, $F_z^g = F_z - mg$, x_e is the Jacobian matrix, total z force, and equilibrium position, respectively. The root finding algorithm was executed until the delta between the current and previous step was below 0.1 mm.

At this point, the numerical model can be integrated into the digital twin; however, this model is computationally very expensive. Inspecting the calculated equilibrium position reveals that the mapping from the focal to equilibrium point is simple [26], and as simple as two sets of polynomial functions. To fit the polynomial functions to the equilibrium position, the equilibrium positions in the region of interest (ROI); $-\lambda \leq y \leq \lambda$ and $-\lambda + r_c \leq z \leq \lambda + r_c$ were calculated with a step size of $\frac{\lambda}{5}$. Then, the polynomial function was fitted to the data set using the Matlab curve fitting toolbox (ver. 3.7); $x_e^y = a_0 + a_1 x_f^y + a_2 x_f^z$ where a_0, a_1 and a_2 are 7.367×10^{-12} , 0.9981, and -6.962×10^{-10} , respectively. $x_e^z = b_0 + b_1 x_f^y + b_2 x_f^z + b_3 (x_e^y)^2 + b_4 x_e^y x_e^z$ where b_0, b_1, b_2, b_3, b_4 are -1.524×10^{-4} , -2.934×10^{-8} , -1.000 , -1.143×10^{-2} , and -2.343×10^{-7} . The r-squared goodness of fit was 0.999 for both cases.

This significantly simplifies the numerical model, guarantees stability within the ROI, and reduces the number of optimization variables. Similarly to the pressure field optimization, the loss function was set as $L = \sqrt{(y_c - y_p^{exp})^2 + (z_c - z_p^{exp})^2}$ where y_c and z_c are the target positions in the y and z axis. $y_p^{exp} = x_e^y(x_f^y, x_f^z) + G(y^{exp} - x_e^y(x_f^y, x_f^z))$ and $z_p^{exp} = x_e^z(x_f^y, x_f^z) + G(z^{exp} - x_e^z(x_f^y, x_f^z))$ are the substituted experimental equilibrium points. The maximum iteration number was set to 25.

Results and Discussion

Pressure Field Optimization

The results for the A:i, A:ii, and A:iii optimizations are as shown in Fig. 2a, b, and c-d, respectively. As shown in Fig. 2(a-d), the phased array perfectly achieves target optimized states in optimal conditions, i.e. numerical simulation (red crosses). The performance of the optimizer in the numerical simulation as evaluated by the sum of square of error (SSE) for the phases are 6.31×10^{-12} and 6.35×10^{-12} for A:i and A:iii, respectively. The amplitude accuracy is also high with 3.59×10^{-5} and 5.01×10^{-5} for A:ii and A:iii, respectively.

The numerically optimum solution works well for target phase optimization in experiments, and the experimental value closely achieves the target as shown in Fig. 2a and c. The experimental phase accuracy, measured in SSE are 0.109, and 0.0963 for A:i and A:iii respectively. The employment of the experimental optimization improves the accuracy to 0.00646 and 0.0617, respectively for A:i and A:iii. However, because the numerical optima performs well in the first place, the improvement is minor.

However, the numerically optimum solution does not apply well for amplitudes in the experimental condition as shown in Fig. 2b and c. The pressure amplitude accuracy measured in SSE is 2.82×10^6 and 2.92×10^6 for A:ii and A:iii, respectively in the experiment. By the employing experimental optimization, the pressure accuracy improves to 1.78×10^3 and 8.47×10^3 for A:ii and A:iii respectively. The A:iii optimizer consistently performs worse than the

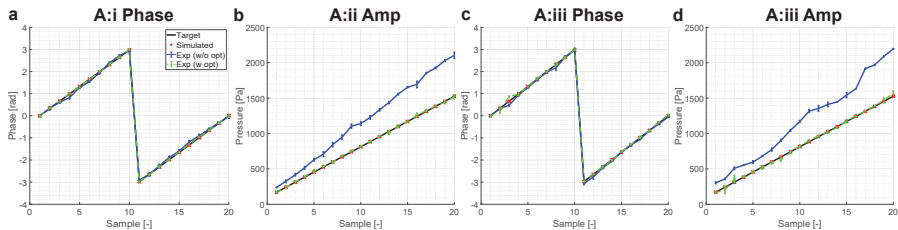


Fig. 2 Comparison of pressure field with numerical optimization only (red x), experimental measurements of numerically optimized solution (blue line with standard deviation), and experimentally optimized value (green dotted line with standard deviation). (a) A:i (phase only hologram with target phase optimization) configuration with its phase performance, (b) A:ii (phase only hologram with target amplitude optimization) configuration with its amplitude performance, (c) A:iii (phase only hologram with target amplitude and phase optimization) configuration with its phase performance and (d) amplitude performance in A:iii configuration. The black line indicates the target for each instance.

counter parts such as A:i or A:ii, and this is attributed to the fact that the loss function is more complex than optimizing for either parameters.

One of the potential cause of the experimental deviation is the nonlinearity of the field. The generation of higher harmonics has been discussed as potential issues by Andrade et al.[21], and it has also been reported to cause issues in underwater acoustics[24]. Fig. 3 shows the measured nonlinearity from the non-optimized field, and Fig. 3a shows that while the third harmonic (F3) stays relatively consistent, the second harmonics generation (F2) enhances as the target amplitude increases. However, when the total harmonic distortion ($\frac{\sqrt{\sum_1^4 (F_n^2)}}{F_1}$) is evaluated up to the fourth harmonic, the distortion decreases with the increased target amplitude. Thus, while the nonlinear effects are present, it does not fully explain the experimental deviation.

Despite the nonlinearity and unknown cause of the experimental deviation, the digital twin optimizer still determines the acoustic holograms for the desired outcome. The in-situ optimization of the pressure amplitude is directly applicable in HCI application (ultrasonic haptic sensation, displays, acoustic streaming), medical applications where the nonlinear and complex media is present in the propagation media, or additive manufacturing where scattering conditions are constantly changing. In-situ optimization can easily be scaled to implement multi-point optimization, and the benefit of in-situ optimization is enhanced with the number of optimization variables and targets. In this case, the experimental measurements may still become the bottleneck in the optimization process, and in such case, efficient measurement methods based on optics (for e.g. schileren[31] or the laser doppler vibrometer[32]) may be better suited for optimization.

Equilibrium Point Optimization

The results are as shown in Fig. 4, and the focal point does not approximate the equilibrium position (RMS error of 0.442 and 0.154 mm), and the optimization process is required. Digital twin optimization was then performed with the

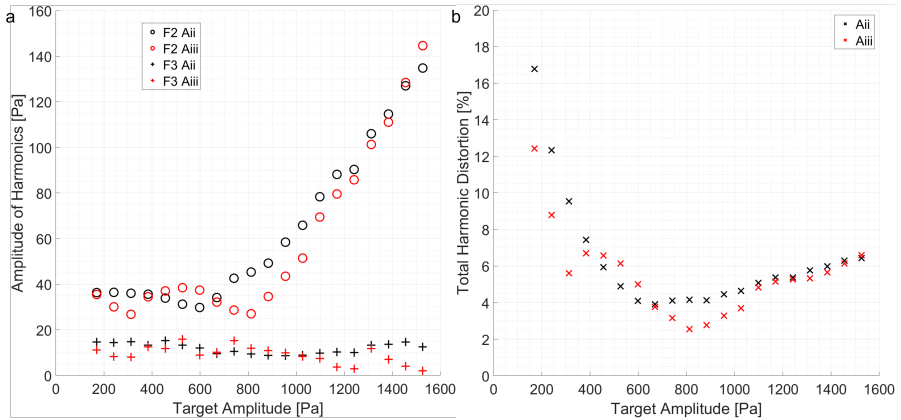


Fig. 3 Investigation of nonlinear effects in pressure field optimization. (a) shows the amplitude of higher harmonics generation for each target amplitudes in fig. 2. The black and red points indicate results from A:ii and A:iii, respectively. The circles and plus indicate the second (80 kHz) and third harmonic (120 kHz) generation respectively. (b) shows the total harmonic distortion for each target amplitude. It starts high but settles to $\approx 6\%$ after target amplitude of 1200 Pa.

Adam optimizer (learning rate = 5×10^{-4}), with the initial solution set as the target focal point ($q = 0$). For subsequent optimization ($q \leq 1$), the initial guess was set to the optimized focal points from the last iteration. The optimizer was iterated for 25 steps, and the results are as shown in Fig. 4. After the experimental optimization, the RMS error dropped to 0.105 and 0.057 mm for the y and z axis respectively, significantly improving the positioning accuracy of the acoustic levitator.

Where previous methods [26] required a calibration map (which typically requires many hours to measure), this in-situ optimizer achieves equivalent performance (RMS of 0.11 and 0.030 mm for horizontal and vertical axes respectively [26]) without the calibration map. Thus, this could be used to improve the image quality in acoustophoretic volumetric displays, or improve positioning in diagnostics/analytic purposes[33–35].

Designing the Loss Function

In-situ optimization has been demonstrated previously in machine learning and optical systems; however, the design of the loss function itself has not been discussed in depth. The design of the loss function is the most critical in achieving a successful experimental optimization with digital twin. This is because we do not identify any derivatives via experiments. The loss function needs to be designed such that the experimental values are passed on to the optimizer; otherwise, the optimizer will only find the numerical optima. This could be a potential pitfall for the future of experimental optimization with the digital twin, and we will present an example where such a design may be critical.

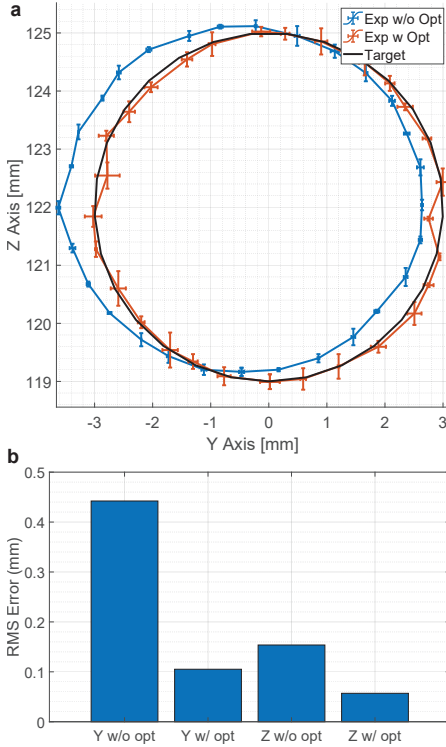


Fig. 4 Results of equilibrium position optimization. (a) shows the absolute position of the target (black), experimental results without optimization (blue), and with optimization (orange). The errorbar indicate the standard deviation. (b) shows the RMS error of the trajectory for each axis with and without optimization.

We set a toy optimization problem where $f_{ideal}(x) = -x^2$, and the experimental deviated function, $f_{exp}(x) = (x - 10)^2$ (see Data Availability for the codes). A simple loss function to obtain the maxima of the function is; $L_1(x) = -f_{ideal}(x)$, $L_2 = -f_{exp}(x)$. Trivially, the solution is $x = 0$, and $x = 10$ for the ideal and experimental case, respectively. We then convert the loss function to include the experimental data and preserve the automatic differentiated value; $L_3 = -(f_{ideal}(x) + G(f_{exp}(x) - f_{ideal}(x)))$. We solved the L_3 with the Adam optimizer (learning rate = 0.1), and obtained the mean optimal points by repeating the optimization 100 times with random initial values between -2.5 and 22.5 (i.e. center at 10).

When such optimization is performed, the function converges only to the numerical optima ($x = 0$). This is because the function only knows the numerical maximum, and the loss function is not properly designed to descend to the target. Thus, for a function to be maximized, the loss function needs to have a steep gradient near the maxima, and still have a term $f(x)$ when differentiated. One such function is $\frac{\delta L_4}{\delta x} = \frac{f'(x)}{f(x)}$, or $L_4(x) = \log f(x) =$

$\log(f_{ideal}(x) + G(f_{exp}(x) - f_{ideal}(x)))$. This is not a perfect maximization function, because (1) the value does not reach the optima when it starts from the left hand side of optima, (i.e. $x \leq 10$ the returned solution has a mean of $x = 0.300$, with a s.t.d. of 1.22, number of instances 54/100) and (2) the solution could be NaN out depending on the initial value; however, the solution improves to a mean of 8.32 (std: 0.491, number of instance 41/100), given a good initial guess ($x \geq 10$). Further study is required to identify more suitable loss or optimizing functions knowledge should be helpful in the future applications of in-situ optimization.

Conclusion

In conclusion, we presented an in-situ optimization method of the acoustic hologram with a digital twin. This optimizer obtains the experimental measurements, and optimized the hologram using experimental measurements and numerical gradients. We demonstrated two approaches for the measurements (microphone, and camera), and two approaches for the modelling (i.e. direct numerical model, and polynomial approximation). Both methods were successful in improving the performance of the hologram. This optimization method, along with the design philosophy for the loss function will be directly helpful in improving the performance of the practical application of PAT.

Methods

Pressure Calculation

The complex pressure at a specific point (x) generated by PAT is calculated by;

$$p_{in}(x, x_t, \phi_t) = \sum_{t=1}^T \frac{P_0}{d(\mathbf{x}, \mathbf{x}_t)} D(\eta) e^{j(kd(\mathbf{x}, \mathbf{x}_t) + \phi_t)}, \quad (6)$$

where P_0 is the transducer power at 1 m, $d(\mathbf{x}, \mathbf{x}_t)$ is the Euclidean distance between the transducer position (x_t) and the specified position (x). $D(\eta) = \frac{2J_1(kr \sin \eta)}{kr \sin \eta}$ is the directivity function for a piston source. $k = \frac{2\pi f_0}{c_0}$ is the wavenumber, with $f = 40$ kHz and $c_0 = 341$ ms⁻¹.

We employed a phased array made of 256 transducers of 1 cm diameter, operating at 40 kHz (Manorshi, MSO-P1040H07T, $P_0 = P_v V_a$, where $P_v = 0.31$ Pa V⁻¹ at 1 m, and $V_a = 5$ V is the actuated voltage) and we refer to SonicSurface for details regarding the signal generation for each transducers)[36]. The transducers are arranged in a 16×16 square flat grid. A field-programmable gate array (FPGA) (EP4CE6E22C8N—ALTERA IV Core Board, Waveshare) generates the control signals multiplexed into 8 channels per output pin, shift registers (74HC595, TI) demultiplex the pin signal into 8 channels, and the channels get amplified by drivers (MIC4127 from MT) up to 20 peak-to-peak voltage. The signals to be generated are sent by a computer to the FPGA using UART at 230,400 bps, enabling to update the emission phases

190 times per second. The phase resolution was 32 divisions per period. The transducer power coefficient was measured by taking the average of 10 transducers, and the microphone was oriented such that the microphone pointed towards the PAT.

Experimental Pressure Field Measurements

The calibrated microphone was connected to the conditioning amplifier (B&K Type 2690), and the output voltage was recorded using the USB oscilloscope (TiePie Handyscope HS5). The captured data were converted from voltage to pressure amplitude based on the calibration data, and the FFT was obtained to determine the amplitude and phase at the fundamental frequency (40 kHz). The reference for the phase was set as the clock signal from the FPGA board. The microphone was attached to the XYZ stage (Controller: OptoSigma SHOT-304GS, Stages: OptoSigma OSMS20-85, OSMS26-100, OSMS26-100) to accurately control the position of the microphone and stage commands were sent via Serial communication (baud rate = 9600) using the pyOptoSigma package¹. The optimization scheme was implemented in Python (ver 3.10.7) and codes to fully recreate the setup were made available as shown in the data availability section (TensorFlow ver. 2.10.0). The adam optimizer was used, the learning rate was 0.05, and the optimizer was iterated 100 times. Experimental measurements and optimizations were repeated three times to obtain the average performance, and its standard deviation, the average accuracy of the phase ($\sum |\phi_c - \phi|$) and pressure ($\sum |A_c - A|$)

Experimental Measurement of Equilibrium Position

The experiment was conducted on top of an optical table (Thorlabs B90120A, SDP90120), and the equilibrium position was captured by a USB-C high speed camera (Photron INFINICAM UC-1) with a Nikon F-to-C Mount Adaptor (Kenko Tokina) and a single-focus lens (Tamron SP AF180mm F/3.5Di). A CMM-stylus (RENISHAW A-5000-7557) was attached to the aforementioned XYZ stages to obtain both the pixel to mm conversion rate (1.408×10^{-5} mm pix⁻¹) and datum point. The camera was operated through Python SDK (pypuclib²), and the equilibrium position and camera calibration was identified using the hough circle transform on OpenCV (ver 4.6.0).

Acknowledgments. This work was supported by JSPS KAKENHI Grant Number JP21K14103. We would like to thank Dr. Azier Marzo and Mr. Iñigo Ezcurdia for their assistance on the experimental setup. The authors would like to acknowledge OpenAI and ChatGPT for the mostly automated generation of the abstract.

¹<https://github.com/ken1row/PyOptoSigma>

²<https://github.com/infinicam/pypuclib>

Declarations

Y.O. has multiple unpaid advisory positions for governmental/non-governmental bodies in Japan.

References

- [1] Hoshi, T., Takahashi, M., Iwamoto, T., Shinoda, H.: Noncontact tactile display based on radiation pressure of airborne ultrasound. *IEEE Transactions on Haptics* **3**, 155–165 (2010). <https://doi.org/10.1109/TOH.2010.4>
- [2] Long, B., Seah, S.A., Carter, T., Subramanian, S.: Rendering volumetric haptic shapes in mid-air using ultrasound. *ACM Transactions on Graphics* **33**, 1–10 (2014). <https://doi.org/10.1145/2661229.2661257>
- [3] Seah, S.A., Drinkwater, B.W., Carter, T., Malkin, R., Subramanian, S.: Dexterous ultrasonic levitation of millimeter-sized objects in air. *IEEE Transactions on Ultrasonics, Ferroelectrics, and Frequency Control* **61**, 1233–1236 (2014). <https://doi.org/10.1109/TUFFC.2014.3022>
- [4] Marzo, A., Seah, S.A., Drinkwater, B.W., Sahoo, D.R., Long, B., Subramanian, S.: Holographic acoustic elements for manipulation of levitated objects. *Nature Communications* **6**, 8661 (2015). <https://doi.org/10.1038/ncomms9661>. NULL
- [5] Ochiai, Y., Hoshi, T., Rekimoto, J.: Three-dimensional mid-air acoustic manipulation by ultrasonic phased arrays. *PLoS ONE* **9**, 97590 (2014). <https://doi.org/10.1371/journal.pone.0097590>
- [6] Hasegawa, K., Qiu, L., Noda, A., Inoue, S., Shinoda, H.: Electronically steerable ultrasound-driven long narrow air stream. *Applied Physics Letters* **111**, 064104 (2017). <https://doi.org/10.1063/1.4985159>
- [7] Norasikin, M.A., Plasencia, D.M., Memoli, G., Subramanian, S.: Sonic-spray: A technique to reconfigure permeable mid-air displays. *ISS 2019 - Proceedings of the 2019 ACM International Conference on Interactive Surfaces and Spaces*, 113–122 (2019). <https://doi.org/10.1145/3343055.3359704>
- [8] Fushimi, T., Marzo, A., Drinkwater, B.W., Hill, T.L.: Acoustophoretic volumetric displays using a fast-moving levitated particle. *Applied Physics Letters* **115**, 64101 (2019). <https://doi.org/10.1063/1.5113467>
- [9] Hirayama, R., Christopoulos, G., Plasencia, D.M., Subramanian, S.: High-speed acoustic holography with arbitrary scattering objects. *Science Advances* **8**, 7614 (2022). <https://doi.org/10.1126/sciadv.abn7614>

- [10] Ochiai, Y., Hoshi, T., Rekimoto, J.: Pixie dust: graphics generated by levitated and animated objects in computational acoustic-potential field. *ACM Transactions on Graphics* **33**, 85 (2014). <https://doi.org/10.1145/2601097.2601118>
- [11] Morales, R., Marzo, A., Subramanian, S., Martínez, D.: Leviprops: Animating levitated optimized fabric structures using holographic acoustic tweezers. *Proceedings of the 32nd Annual ACM Symposium on User Interface Software and Technology*, 651–661 (2019). <https://doi.org/10.1145/3332165.3347882>
- [12] Melde, K., Mark, A.G., Qiu, T., Fischer, P.: Holograms for acoustics. *Nature* **537**, 518–522 (2016). <https://doi.org/10.1038/nature19755>
- [13] Marzo, A., Drinkwater, B.W.: Holographic acoustic tweezers. *Proceedings of the National Academy of Sciences* **116**, 84–89 (2018). <https://doi.org/10.1073/pnas.1813047115>
- [14] Plasencia, D.M., Hirayama, R., Montano-Murillo, R., Subramanian, S.: Gs-pat: High-speed multi-point sound-fields for phased arrays of transducers. *ACM Trans. Graph.* **39** (2020). <https://doi.org/10.1145/3386569.3392492>
- [15] Lin, Q., Wang, J., Cai, F., Zhang, R., Zhao, D., Xia, X., Wang, J., Zheng, H.: A deep learning approach for the fast generation of acoustic holograms. *The Journal of the Acoustical Society of America* **149**, 2312–2322 (2021). <https://doi.org/10.1121/10.0003959>
- [16] Lee, M.H., Lew, H.M., Youn, S., Kim, T., Hwang, J.Y.: Deep learning-based framework for fast and accurate acoustic hologram generation. *IEEE Transactions on Ultrasonics, Ferroelectrics, and Frequency Control* **69**, 3353–3366 (2022). <https://doi.org/10.1109/TUFFC.2022.3219401>
- [17] Li, J., Lv, Z., Hou, Z., Pei, Y.: Comparison of balanced direct search and iterative angular spectrum approaches for designing acoustic holography structure comparison of balanced direct search and iterative angular spectrum approaches for designing acoustic holography structure. *Applied Acoustics* **175**, 107848 (2020). <https://doi.org/10.1016/j.apacoust.2020.107848>
- [18] Suzuki, S., Fujiwara, M., Makino, Y., Shinoda, H.: Radiation pressure field reconstruction for ultrasound midair haptics by greedy algorithm with brute-force search. *IEEE Transactions on Haptics* **14**, 914–921 (2021). <https://doi.org/10.1109/TOH.2021.3076489>
- [19] Fushimi, T., Yamamoto, K., Ochiai, Y.: Acoustic hologram optimisation using automatic differentiation. *Scientific Reports* **11**, 12678 (2021). <https://doi.org/10.1038/s41598-021-01267-8>

[//doi.org/10.1038/s41598-021-91880-2](https://doi.org/10.1038/s41598-021-91880-2)

- [20] Fushimi, T., Yamamoto, K., Ochiai, Y.: Target acoustic field and transducer state optimization using diff-pat. *AIP Advances* **11**, 125007 (2021). <https://doi.org/10.1063/5.0069182>
- [21] Andrade, M.A.B., Ramos, T.S., Okina, F.T.A., Adamowski, J.C.: Nonlinear characterization of a single-axis acoustic levitator. *Review of Scientific Instruments* **85**, 045125 (2014). <https://doi.org/10.1063/1.4872356>
- [22] Prisbrey, M., Raeymaekers, B.: Ultrasound noncontact particle manipulation of three-dimensional dynamic user-specified patterns of particles in air. *Physical Review Applied* **10**, 034066 (2018). <https://doi.org/10.1103/PhysRevApplied.10.034066>
- [23] Paneva, V., Fleig, A., Plasencia, D.M., Faulwasser, T., Müller, J.: Optitrap: Optimal trap trajectories for acoustic levitation displays. *ACM Transactions on Graphics* **41**, 1–14 (2022). <https://doi.org/10.1145/3517746>
- [24] Sallam, A., Shahab, S.: On nonlinear effects in holographic-modulated ultrasound. *Applied Physics Letters* **121**, 204101 (2022). <https://doi.org/10.1063/5.0123271>
- [25] Polychronopoulos, S., Memoli, G.: Acoustic levitation with optimized reflective metamaterials. *Scientific Reports* **10**, 4254 (2020). <https://doi.org/10.1038/s41598-020-60978-4>
- [26] Fushimi, T., Marzo, A., Hill, T.L., Drinkwater, B.W.: Trajectory optimization of levitated particles in mid-air ultrasonic standing wave levitators. 2018 IEEE International Ultrasonics Symposium (IUS), 1–9 (2018). <https://doi.org/10.1109/ULTSYM.2018.8580093>
- [27] Wright, L.G., Onodera, T., Stein, M.M., Wang, T., Schachter, D.T., Hu, Z., McMahon, P.L.: Deep physical neural networks trained with backpropagation. *Nature* **601**, 549–555 (2022). <https://doi.org/10.1038/s41586-021-04223-6>
- [28] Peng, Y., Choi, S., Padmanaban, N., Wetzstein, G.: Neural holography with camera-in-the-loop training. *ACM Trans. Graph. (SIGGRAPH Asia)* **39**, 1–14 (2020). <https://doi.org/10.1145/3414685>
- [29] Gor'kov, L.P.: On the forces acting on a small particle in an acoustical field in an ideal fluid. *Soviet Physics Doklady* **6**, 773 (1962)
- [30] Bruus, H.: Acoustofluidics 7: The acoustic radiation force on small particles. *Lab on a Chip* **12**, 1014–1021 (2012). <https://doi.org/10.1039/>

c2lc21068a

- [31] Contreras, V., Marzo, A.: Adjusting single-axis acoustic levitators in real time using rainbow schlieren deflectometry. *Review of Scientific Instruments* **92**, 015107 (2021). <https://doi.org/10.1063/5.0013347>
- [32] Malkin, R., Todd, T., Robert, D.: A simple method for quantitative imaging of 2d acoustic fields using refracto-vibrometry. *Journal of Sound and Vibration* **333**, 4473–4482 (2014). <https://doi.org/10.1016/j.jsv.2014.04.049>
- [33] Puskar, L., Tuckermann, R., Frosch, T., Popp, J., Ly, V., McNaughton, D., Wood, B.R.: Raman acoustic levitation spectroscopy of red blood cells and plasmodium falciparum trophozoites. *Lab on a Chip* **7**, 1125 (2007). <https://doi.org/10.1039/b706997a>
- [34] Yurduseven, O., Cooper, K., Chattopadhyay, G.: Point-spread-function (psf) characterization of a 340-ghz imaging radar using acoustic levitation. *IEEE Transactions on Terahertz Science and Technology* **9**, 20–26 (2019). <https://doi.org/10.1109/TTHZ.2018.2876418>
- [35] Chen, X., Ding, Q., Bi, C., Ruan, J., Yang, S.: Lossless enrichment of trace analytes in levitating droplets for multiphase and multiplex detection. *Nature Communications* **13**, 7807 (2022). <https://doi.org/10.1038/s41467-022-35495-9>
- [36] Morales, R., Ezcurdia, I., Irisarri, J., Andrade, M.A.B., Marzo, A.: Generating airborne ultrasonic amplitude patterns using an open hardware phased array. *Applied Sciences (Switzerland)* **11** (2021). <https://doi.org/10.3390/app11072981>